First Resolved Observations of the Demagnetized Electron-Diffusion Region of an Astrophysical Magnetic-Reconnection Site

J. D. Scudder, R. D. Holdaway, W. S. Daughton, H. Karimabadi, V. Roytershteyn, C. T. Russell, and J. Y. Lopez

First Resolved Observations of the Demagnetized Electron Diffusion Region

J.D. Scudder[1], R.D. Holdaway[1], W. S. Daughton[2], H. Karimabadi[3], V. Roytershteyn[3], C.T. Russell[4], and J.Y. Lopez[1]

[1] *University of Iowa, Iowa City, IA 52442;* [2] *Los Alamos National Labs, Los Alamos, NM 87544;*
[3] *UCSD, La Jolla, CA 92093;* [4] *UCLA, Los Angeles, CA 90095*

Spatially resolved, diagnostic signatures across the X-line and Electron Diffusion Region (EDR) by the Polar spacecraft are reported at the Earth's magnetopause. The X-line traversal has a local electron's skin depth scale. First resolved EDR profiles are presented with peak electron thermal mach numbers > 1.5 , anisotropy > 7, calibrated electron agyrotopy > 1 and misordered expansion parameters indicative of demagnetization and strong (150eV) increases in electron temperature. The amplitude and phase of these profiles correlate well with a guide geometry kinetic simulation of collisionless magnetic reconnection. Such high resolution diagnosis has been made possible by data processing techniues that afford an 11 fold reduction in the aliasing time for the electron moments.

Astrophysical energy releases, like solar flares, aurorae and substorms, have been attributed since 1946 [1] to topological reorganizations of preexisting magnetic structures in plasmas permitted by localized dissipation in current channels. This reorganization, called "magnetic reconnection," is facilitated in laboratory plasmas by binary collisions. For nearly collisionless astrophysical plasmas the direct relevance of magnetic reconnection initially remained unclear. In 1975 a theoretical description for collisionless reconnection [2] was introduced that suggested the topology changes can occur at (i) current layers approaching the scale of the thermal electron gyroradius, ρ_e, where (ii) non-ideal corrections to the electron pressure tensor allow the frozen flux condition to be overcome. These considerations, involving the demagnetization of the electrons, suggested a current channel, called the Electron Diffusion Region (EDR), would form in this process with scales of *order* $d_i \times d_e$ where the k'th species skin depth is $d_k \equiv (\frac{m_k c^2}{4\pi n e^2})^{1/2}$. In a plasma with equal electron, ion and magnetic pressures the EDR would have scales of order $\rho_i \times \rho_e$ where $\rho_k = \frac{w_k}{\Omega_{ck}}$ and w_k and Ω_{ck} are the thermal speed and cyclotron frequency of the k'th species, respectively. The extent of electron demagnetization is reflected in the broken cylindrical symmetry of the electron pressure tensor, $\mathbf{P}_e$, about the magnetic field; a *measure* of this broken symmetry, called agyrotropy, is denoted by $A\emptyset_e$ [3]. In typical, large scale plasmas demagnetization of electrons does not occur and $A\emptyset_e \simeq 0$ is the accepted, integrated statement of magnetization of electrons. In the last decade it has become possible to provide computational support for collisionless reconnection by using large scale Particle in Cell (PIC) simulations [4], often with artificial particle masses, cyclotron to plasma frequency ratio, and idealized boundary conditions. Observational signatures, such as Alfvenic acceleration layers, parallel electric fields or keV electron fluxes, have been interpreted as *circumstantial* evidence of detection of reconnection (or even the EDR) in the solar wind, earth's magnetosheath and planetary magnetopauses [5–7].

We report the first *in situ* quantitative evidence for demagnetized thermal electrons within a resolved EDR in a collisionless astrophysical plasma. The detection uses five independent determinations, from 3 independent instrument suites [8], of the relevant short scales and integral measures of electron demagnetization that are the essential ingredients how reconnection would be possible in low density plasmas [2]. All 5 measured profiles are supported in size *and* spatial phasing by PIC simulations with similar dimensionless parameters. These signatures have such singularly large values, that in over 50 years of space plasma measurements they have never occurred separately, let alone in concert, as in this identification. These signatures reflect a plasma regime unique to collisionless reconnection, as benchmarked in the PIC simulations [9]. A recent 11 fold reduction in time aliasing of the Polar plasma instrument's computation of 3D moments has allowed a greatly clarified diagnosis of the moving, electron gyroscale structures involved. Since the needed plasma moments [10] involve averages over only low order velocity space Spherical Harmonics, Y_l^m with $l \leq 2$, relatively low order Laguerre Spherical Harmonic fits can determine these moments from data acquired over 1.15s from the instrument's unique, simultaneous sampling in all octants of velocity space. [11].

The definitions and origin of the five dimensionless, scalar diagnostics used to find the EDR are distinct from those circumstantial signatures of reconnection/EDR previously used in the experimental literature. Together with the electromagnetic field they involve either the electron bulk velocity, $\mathbf{U}_e$, and/or derived parameters, such as the pressure tensor, determined in the electron rest frame. They are:

(i) *energy gain per cyclotron period*, $\epsilon_e \equiv \frac{2\pi e \mathbf{E} \cdot \mathbf{U_e}}{\Omega_{ce} k T_e}$, which is an expansion parameter of Guiding Center Theory (GCT) [9]; (ii) *relative strength of electric and magnetic force in the electron fluid rest frame*, $\delta_e \equiv \frac{|c\mathbf{E} + \mathbf{U_e} \times \mathbf{B}|}{w_{e\perp} B} \simeq \frac{\rho_e}{L}$, another GCT expansion parameter [9]; (iii) *agyrotropy of the measured electron pressure tensor*,
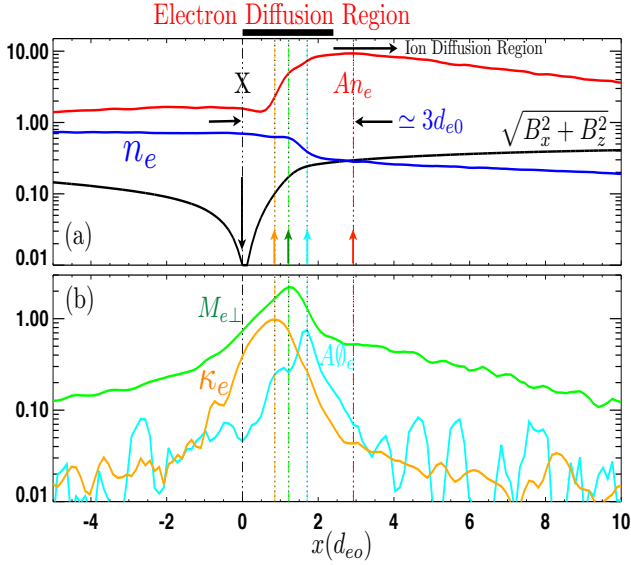
FIG. 1: PIC Profiles through Electron Diffusion Region (indicated by thick horizontal black bar) passing through the separator (x=0) showing (a) profiles of An_e (red), n_e (blue) and the in plane field components of **B** (black), and (b) PIC diagnostics of electron inertial scale physics: $A\emptyset_e$ (cyan), $M_{e\perp}$ (green), and composite Guiding Center Theory violation of expansion parameters, κ_e (orange). Arrows at peaks of same colored profiles. Phasing of peaks of $X, M_{e\perp}, A\emptyset_e, An_e$ are shown in Polar data in Figure 3R.
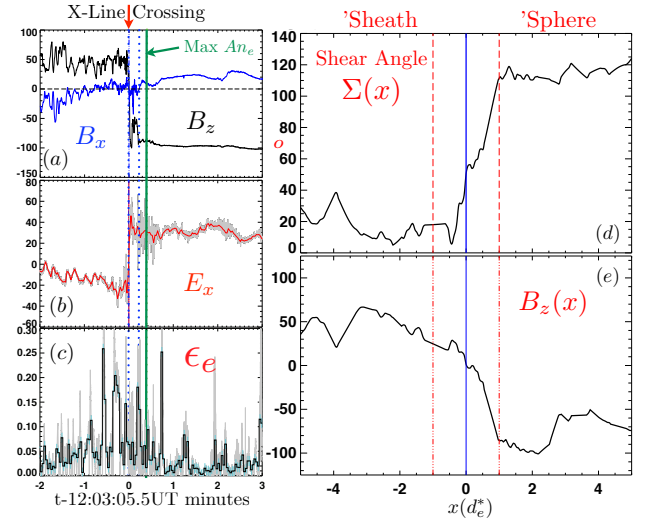

FIG. 2: *In situ*: observations *Left column*: *time profile* X-line vicinity in NIF, Minimum Faraday Residue coordinates showing measured (a) normal and shear magnetic components, $B_x(t)$, $B_z(t)$, (b) the normal electric component: $E_x(t)$ and (c) $\epsilon_e(t)$, the *measured* rate of work being done on the electrons per gyro period scaled by kT_e. *Right*: Illustrates *spatial profile* of (d) the resolved X-line shear angle, $\Delta\Sigma(x) \simeq 120^o$, and (e) interconnecting $B_z(x)$ variations within $\pm 5d_e^*$ about the separator X-line. Asterisk denotes cumulative number of such units from the X-line, $d_e^* = 0$. Grey shadows indicate variances about averages.

$A\emptyset_e = 2\frac{|1-\alpha|}{(1+\alpha)} > 1$ (where $\alpha \equiv P_{e\perp,1}/P_{e\perp 2}$ is the ratio of possibly distinct eigenvalues transverse to **B** [3]); (iv) *electron thermal anisotropy*, $An_e \equiv \frac{T_{e,\parallel}}{<T_{e,\perp}>}$ lining the interface between the EDR and magnetospheric Ion Diffusion Region (IDR) [12]; and (v) *large electron thermal mach number*, $M_{e,\perp} \equiv \frac{|\mathbf{U}_e|}{<w_{e,\perp}>} \simeq O(1)$ [9], reflecting the needed ρ_e current channel of the EDR, where $<w_{e,\perp}>$ is the electron thermal speed derived from the average perpendicular temperatures. We define κ_e to be the larger local value between δ_e and ϵ_e. It is also of interest that ϵ_e can depend on the *perpendicular and parallel* components of **E**, especially when the electrons are demagnetized. A sixth correlative signature that is expected for the EDR, but not unique to demagnetization physics, is increased internal or suprathermal energy stored in the electrons.

From a 2D PIC simulation in the asymmetric guide geometry we show in Figure 1 an illustrative spatial profile through the magnetic separator and across the EDR-IDR. The simulation had a guide field equal to the reconnecting field on the stronger field side of the layer, used $T_i/T_e = 1$, $\frac{m_i}{m_e} = 100$, $\frac{\omega_{pe}}{\Omega_{ce}} = 2$, $\beta_{hi} = 1$ and $\beta_{lo} = 0.125$, where hi(lo) refer to the density of the asymmetric configuration. The equilibrium was achieved by the recently described method [13]. The separator (X-line) crossing $(x \equiv 0)$ occurs where the reconnecting and normal components of **B** simultaneously vanish (inset(a)). Enhanced An_e requires adiabatic/magnetized electrons; thus, the

peak of An_e (inset 1(a)) occurs just outside of the EDR-IDR interface, suggesting an EDR width of $\leq 3d_{eo}$. The signatures of demagnetized electrons (inset 1(b)) straddle the EDR, producing ordered enhancements of $\kappa_e \simeq 1$, $M_{e,\perp} \simeq 2$, $A\emptyset_e \simeq 0.75$, and $An_e \simeq 7-8$, upon crossing the EDR-IDR boundary. The An_e profile extends asymmetrically into the magnetospheric IDR, but is sharply attenuated on the separator side. $An_e(x)$ is sharply reduced when $A\emptyset_e$ peaks. The peak of $M_{e\perp}$ is closer to the magnetosheath than the peak of $A\emptyset_e$. The GCT violations reflected in $\kappa_e \neq 0$ peak closer to and extend over the separator layer towards x=-1. Non-ideal effects are seen at the separator, but the most intense signatures of demagnetization $(M_{e,\perp}, A\emptyset_e)$ occur toward the rear of the EDR, nearer to the low density IDR boundary.

The reported event occurred near noon on May 4, 1998, as NASA's Polar spacecraft traversed the sunlit magnetopause at $9.0R_e$ at a magnetic latitude of 74.47^o. As is typical at the magnetopause, the crossing had density and magnetic field strength asymmetries. Its guide magnetic field component was comparable to its shearing component and the layer encompassed a shear angle of 120°. The magnetic separator was observed straddling 12:03:05.5UT, as shown versus time (space) in the left (right) column of Figure 2. Insets 2(a-c) support this identification, showing simultaneous (a) nulling of the shearing (z) and normal (x) components of **B**, at the

location (b) of strongly convergent normal component of E_x. Components are shown in a NIF Minimum Faraday Residue frame [14, 15]. Within ($\pm 40s$) of the identified separator crossing, framing signatures of enhanced energy transfer, $\epsilon_e \simeq 0.25$ to the electrons is demonstrated and to be distinguished from the low values surrounding this region.

The relative velocity (1.6 km/s) of disturbances relative to the spacecraft was determined by the Faraday Residue method [14], which permitted estimates of spatial distances used in insets 2(d) and 2(e). The magnetic shear angle, $\Sigma(x) \equiv cos^{-1}(\hat{\mathbf{b}}(\mathbf{x}) \cdot \hat{\mathbf{b}}_{\mathbf{o}})$, advances in an orderly manner through 120° on the electron inertial scale, (inset 2(d)) within $\pm d_e^*$ of the separator, where d_e^* is one cumulative *local* electron skin depth from of the separator, $d_e^* \equiv 0$. As theoretically expected the B_z shearing components (inset 2(e)) decrease linearly with distance at different (β_e dependent) rates on either side towards zero.

The 1 hour plasma context surrounding the *in situ* separator crossing of Figure 2 is shown in the left hand (L) column of Figure 3. Initially in the magnetosheath, the spacecraft decisively enters the magnetosphere after 12:06UT. Several different lines of evidence suggest that the relative motion of the spacecraft before and after this magnetopause transit is *not* monotonic. Atypically large $An_e > 7$ is seen between 12:02:30-12:04:30, while spikes of An_e and other variables (Figure 3L) occur earlier and later than this time. A portion of the apparent time variability of the derived parameters may be caused by the non-uniform proximity and non-monotonic advance of the spacecraft towards (away) from the sharp, d_e scaled separator shown in Figure 2.

The very strong peak of $An_e(x)$ in the PIC profile in Figure 1 and the large variations of $An_e(t)$ of Figure 3L suggest using the wide swings of the observed $An_e(t)$ to reorder the temporal measurements. The mapping uses $An_e(t)$ to produce inset 3(b) from inset 3(a). The rule divides the chronologically ordered *vector* $\mathbf{V}$, with elements $V_i = An_e(i\Delta t)$, into two smaller vectors $\mathbf{V_1}, \mathbf{V_2}$ whose elements are respectively those of $\mathbf{V}$ for $i \leq k^*$ and $i > k^*$, respectively, where k^* is the index of the highest value of An_e within the strong ramp seen in the density in inset 3(i). The components of $\mathbf{V_1}$ are sorted to be monotonic increasing in successive elements of the sorted vector $\mathbf{SV_1}$, while $\mathbf{V_2}$ is sorted into $\mathbf{SV_2}$ on the basis of monotonic decreasing size of $An_e(i > k*)$. The result of the rule is the composite vector $\mathbf{SV} \equiv \mathbf{SV_1} \oplus \mathbf{SV_2}$, which is plotted in *its* index order in inset 3(b). The rule between inset 3(a)-3(b) is a map of indices i from the time domain variable to resorted indices $j(i)$ that can be used for any quantity measured with the same time cadence as $An_e(t)$. From this construction, it is clear that the *means* and *extremes* of $\mathbf{V_j}$ and $\mathbf{SV_j}$ are the same as illustrated between insets 3(i) and (j).

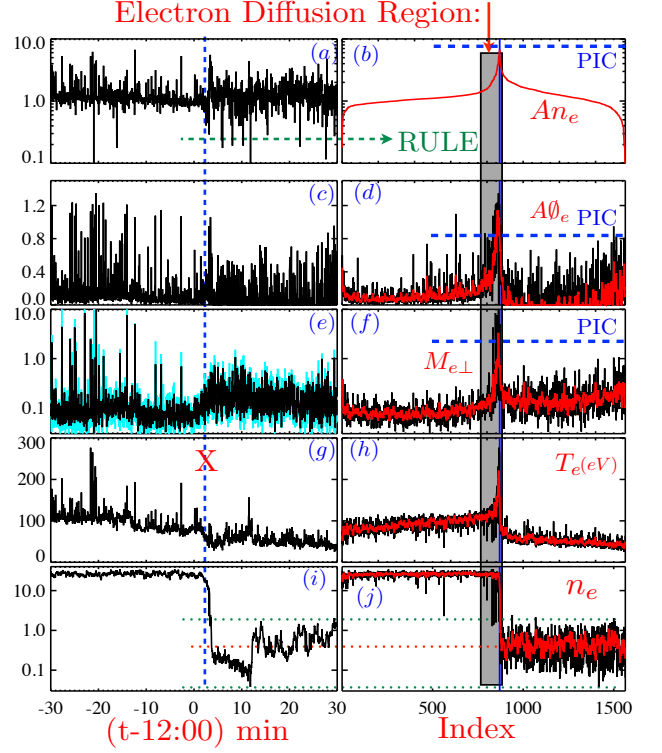Under this rule the horizontal axis of Figure 3L would

FIG. 3: Derived *electron* parameters across separator and EDR. **L** column presents data in time order with X-line indicated by the vertical dotted blue line at 12:03:05.5UT. Panels in **R** column are organized by a "Rule" that reorders spectra indices by their increasing size of An_e to the left of the peak and, with decreasing order to the right, producing the *smooth* single peaked An_e profile in (b). Rule explained in text. This rule changes the temporal order in the left column, making smooth juxtapositions of similar An_e in the right column. The EDR is associated with the shaded rectangle in right column, where coherent signatures of demagnetization, heating of electrons and gyroscales are reenforced by this organization and achieve levels (horizontal dashed blue lines) predicted by PIC. Black traces are data at highest resolution. Red traces are smoothed trends of black traces. Cyan shadowing in Figure 3(e) reflects $\pm 3\sigma$ uncertainties.

become a monotonic, but non-uniform, spatial coordinate for Figure 3R *if* $An_e(x)$ were known to be monotonic in space on either side of its peak value (blue vertical line). From Figure 1 the PIC An_e profile is only slightly non-monotonic near the separator, but *is* monotonic throughout most of the EDR, including its extremely large values when $An_e >> 1$. This rule juxtaposes similar regimes of An_e and allows an experimental assay of the spatial phasing of other observables with respect to the peak of An_e. At lower values of anisotropy, especially where $An_e < 1$, the rule for the x axes of Figure 3R separates spatial layers having large ∇An_e that might spatially be very "close" to those of high An_e.

The rule maps within rows the black curves of Figure 3L into the black curves in Figure 3R. Localized but

sharp transitions are revealed in Figure 3R in the electron observables: strong narrow peaks in with (i) mean energy $T_e \simeq 300eV$, (ii) $An_e \simeq 8$, (iii) $M_{e\perp} \simeq 1.5$, (iv) $A\emptyset_e > 1$, and a newly clarified step in the density (inset 3(i)→3(j)) astride the maximum An_e peak, consistent with the PIC profiles of Figure 1. The general coherence and reduced structure of the panels in Figure 3R suggests that much of the spikiness of the left hand column of Figure 3 is *not* caused by the new method which has improved the plasma data's time resolution 11 fold [10].

The coherence produced in Figure 3R warrants the smoothing (red curves) to compare trends. The *peak* of the trends of $M_{e\perp}$ and $A\emptyset_e$ lead by index number that of the vertical blue line (An_e), consistent with the order suggested by PIC Figure 1(b). The *levels* of the coherent demagnetization signatures compare favorably with those from PIC (dashed horizontal blue lines). Two degenerate candidates emerge for the wide swings in the higher time resolution measurements of Figure 3L: (i) multiple encounters with one cohesive narrow structure induced by changing relative velocities of spacecraft and magnetopause during the crossing, and (ii) encounters with many smaller structures with similar plasma properties. The separatrices emanating from the EDR in PIC are often different from the usual, large radius of curvature "X" patterns of theoretical cartoons. Figures 3L,3R admit the interpretation of multiple encounters with EDR-like properties for a lengthy period both prior to and after the irreversible entry into the magnetosphere. Alternatively, recent 3-D simulations of reconnection [16] have suggested that the EDR spawns multiple current channels, making crossings likely of many very narrow, possibly self-similar fiber-like layers from the main EDR layer.

The coherence within the shaded region of Figures 3R constitutes direct experimental support for non-ideal electron effects as enabling demagnetized thermal electrons in the current channel. The phase coherent signature of large $An_e > 7$ layers with peak amplitudes comparable to that in PIC (dashed blue line Figure 3R(b)), together with the simulation overview that such layers *mark* the EDR-IDR boundary on the magnetospheric side of asymmetric layers, provides further strong support for our EDR identification from adjacent demagnetized layers seen in the shaded rectangle in Figure 3R. The sharply enhanced electron temperature (at the boundary) in the shaded layer is nearly 150eV higher than the larger of the two asymptotic temperatures, representing the first detection of electron heating associated with traversal of a documented reconnection site, and should be contrasted with its reported absence in interplanetary events interpreted to be those of reconnection [6]. The present analysis also provides possible support for the emerging view in 3D simulations that the EDR layer may bifurcate into many smaller demagnetized current channels that Polar

may have intercepted in Figure 3L. The An_e ordering afforded in Figure 3R suggests new ways to organize the emerging 3D picture of reconnection. The detection of the elusive signatures of electron heating and extreme electron $P_{e\parallel} >> P_{e\perp}$ anisotropy confirm the role of parallel potentials and electron trapping physics in the EDR and its proximity [12].

Five observed diagnostics, using three autonomous experiments on the Polar spacecraft have been shown to coordinate well with the amplitude, phase and extent of simulation spatial profiles known to describe the process of collisionless reconnection. The extraordinarily high thermal mach numbers, anisotropy and agyrotropy are so singular in the history of space physics that they require a singular phenomena to explain them. These signatures constitute strong direct experimental evidence of the first detection of the non-ideal demagnetized EDR in a collisionless astrophysical plasma.

[1] R. G. Giovanelli, Nature **158**, 81-82 (1946).
[2] V. M.. Vasyliunas, Rev. Geophys. and Sp. Physics **13**, 303 (1975).
[3] J. D. Scudder and W. Daughton, J. Geophys. Res. **113**, A06222 (2008).
[4] M. Hesse, et al., Phys. Plasma **6**, 1781 (1999); P. L. Pritchett, J. Geophys. Res. **106**, 3783 (2001); W. Daughton, et al., Phys. Plasma **13**, 072101 (2006); H. Karimabadi,et al., Geophys. Res. Lett. **34**, L13104 (2007).
[5] G. Paschmann, Geophys. Res. Letts. **35**, L19109 (2008), and references therein.
[6] J. T. Gosling, SSRv, DOI:10.1007/s11214-0, (2011).
[7] F. S. Mozer, et al., J. Geo. Res. **116**, A12224, (2011).
[8] C.T. Russell, ed., *The Global Geospace Mission*, Kleuwer Academic, New York, New York, 459-495, 563-582, 583-596 (1995).
[9] J. D. Scudder, et al. Phys. Plasma, (in preparation).
[10] See Supplemental Material at [URL will be inserted] for description of the method.
[11] J. D. Scudder,et al., Adv. Sp. Res. **71**, 459-495 (1995).
[12] A. Le, et al., Geophys. Res. Lett. **37**, L03106 (2010).
[13] V. Roytershteyn, Phys. Rev. Lett. (2012).
[14] A. Khrabrov and B. U. 0. Sonnerup, Geo. Res. Letts. **25**, 2373 (1998).
[15] C. C. Goodrich and J. D. Scudder, J. Geophys. Res. **89**, 6654 (1984).
[16] W. Daughton,et al. NatPhys, **7**, 539D (2011).